RSC Sustainability

ROYAL SOCIETY OF CHEMISTRY

ROYAL SOCIETY OF CHEMISTRY

## Sustainability Spotlight Statement

Hydrogenation of carbon dioxide ($CO_2$) to methane ($CH_4$) or methanol ($CH_3OH$) is a promising route to use $CO_2$ as feedstock, lowering its emissions and reducing dependence on fossil fuels. It aligns well the UN's Sustainable Development Goals on energy, sustainability and climate. This study reports the synthesis of copper-based catalysts supported on zinc oxide or graphene, promoted by palladium. The nanoparticles catalysts demonstrate high efficiency in $CO_2$ and CO hydrogenation, favouring methane production at lower metal loadings but methanol production at higher copper content. This sustainable approach highlights the potential for reducing environmental impact by improving catalytic performance.

Please do not adjust margins

# ARTICLE

## Bimetallic CuPd Nanoparticles Supported on ZnO or Graphene for CO$_2$ and CO Conversion to Methane and Methanol

Qaisar Maqbool[a,‡], Klaus Dobrezberger[a,‡], Julian Stropp[a], Martin Huber[a], Karl-Leopold Kontrus[a], Anna Aspalter[a], Julie Neuhauser[a], Thomas Schachinger[b], Stefan Löffler[b], and Günther Rupprechter[a]*

Carbon dioxide (CO$_2$) and carbon monoxide (CO) hydrogenation to methane (CH$_4$) or methanol (MeOH) is a promising pathway to reduce CO$_2$ emissions and to mitigate dependence on rapidly depleting fossil fuels. Along these lines, a series of catalysts comprising copper (Cu) or palladium (Pd) nanoparticles (NPs) supported on zinc oxide (ZnO), as well as bimetallic CuPd NPs supported on ZnO or graphene were synthesized via various methodologies. The prepared catalysts underwent comprehensive characterization via high-resolution transmission electron microscopy (HRTEM), energy-dispersive X-ray spectroscopy (EDX) mapping, electron energy loss spectroscopy (EELS), X-ray diffraction (XRD), hydrogen temperature-programmed reduction and desorption (H$_2$-TPR, -TPD), and deuterium temperature-programmed desorption (D$_2$O-TPD). In the CO$_2$ hydrogenation process carried out at 20 bar and elevated temperatures (300 to 500°C), Cu, Pd, and CuPd NPs (<5wt.% loading) supported on ZnO or graphene predominantly yielded CH$_4$ as primary product, with CO generated as a byproduct via the reverse water gas shift (RWGS) reaction. For CO hydrogenation between 400 and 500°C , the CO conversion was at least 40% higher than that of CO$_2$ conversion, with CH$_4$ and CO$_2$ identified as main products, the latter from water gas shift. Employing 90wt.% Cu on ZnO led to an enhanced CO conversion of 14%, with the MeOH yield reaching 10% and the CO$_2$ yield reaching 4.3% at 230°C. Overall, the results demonstrate that lower Cu/Pd loading (<5wt.%) supported on ZnO/graphene favored CH$_4$ production, while higher Cu content (90wt.%) promoted MeOH production, both for CO$_2$ and CO hydrogenation at high pressure.

## Introduction

Carbon dioxide (CO$_2$) is Earth's most abundant greenhouse gas responsible for absorbing and radiating heat[1]. As of April 2024, the atmospheric CO$_2$ concentration observed by the NOAA Global Monitoring Lab reached 425.38 ppm, marking a new record[2]. This value surpasses any previous levels observed in human history and it is expected to increase to ≈ 500 ppm in the next 20 years, which is regarded as point of no return[3]. Accordingly, the International Energy Agency (IEA) took the initiative of Carbon Capture, Utilization and Storage (CCUS)[4] and Net Zero Emissions by the 2050 (NZE)[5] Scenario. However, despite the existence of numerous strategies, effective solutions to this challenge remain elusive.

The increase in CO$_2$ concentration is largely attributed to burning fossil fuels for energy generation and use as feedstock for chemicals. The utilization of CO$_2$ as an alternative and sustainable carbon source has thus gained worldwide attention as a key aspect of CCUS[6]. The advancements in energy-efficient catalytic CO$_2$ conversion using renewable energy have the potential to mitigate CO$_2$ emissions and reduce reliance on fossil fuels[7]. One of the straightforward ways to utilize CO$_2$ is its hydrogenation to produce value-added products such as hydrocarbons (including olefins, liquid hydrocarbons, and aromatics), oxygenates (such as alcohols and dimethyl ether) or reaction gases such as CO (for syngas, Fischer-Tropsch) or methane[8,9]. The three primary catalytic methods for CO$_2$ hydrogenation include thermal catalysis[8,9,18–20,10–17], electrocatalysis[21,22], and photocatalysis[23–26]. Although thermal catalysis requires higher temperatures and pressures for CO$_2$ activation, it remains a widely applied process for rapid and efficient transformation of CO$_2$ (that could originate from carbon capture).

Due to thermodynamic limitations, reaction to methanol (MeOH) demands high-pressure and elevated operating temperature to achieve proper reaction kinetics, as well as an effective and active catalyst. In this regard, various catalytic materials including Pt, In, Ni, Ru, Zr, Rh, Ga have been widely explored for CO$_2$ hydrogenation to MeOH[27–32]. However, Cu still stands out as the most utilized and studied metal [13–15] due to its high activity at lower temperatures, making it particularly suitable for the CO$_2$ hydrogenation reaction. Additionally, Cu offers advantages in terms of cost-effectiveness, as well as its multivalency (Cu$^0$, Cu$^I$, Cu$^{II}$)[16]. Moreover, Cu maintains stable interaction with oxygen,

[a.] Institute of Materials Chemistry, TU Wien, Getreidemarkt 9/BC, 1060 Vienna, Austria.
[b.] University Service Center for Transmission Electron Microscopy, TU Wien, Stadionallee 2/057-02, 1020 Vienna, Austria
‡ Authors with equal contributions
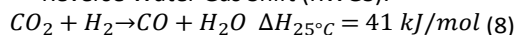*Correspondence: guenther.rupprechter@tuwien.ac.at

**ARTICLE**

preventing the formation of unstable intermediates or surface poisoning. CO-induced mobility of Cu atoms may counteract sintering(33,34). It also exhibits strong interactions with other materials, such as Zn, which improves stability, selectivity, and the ability to dissociate $H_2$(35,36).

Industrially, MeOH is mainly synthesized by a feed of $CO_2$, CO, and $H_2$ at high pressure (100 bar), using $Cu/ZnO/Al_2O_3$ catalysts(37,38). The kinetics and thermodynamics of this reaction have been widely studied(19,39–41) along with the influence of water on catalyst performance (42–44). There are three main reactions involved in the hydrogenation of $CO_2$,
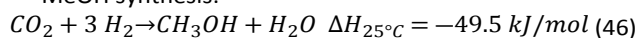
Reverse Water Gas Shift (RWGS):
$$CO_2 + H_2 \rightarrow CO + H_2O \quad \Delta H_{25°C} = 41\ kJ/mol \quad (8)$$
Methanation:
$$CO_2 + 4\ H_2 \rightarrow CH_4 + 2\ H_2O \quad \Delta H_{25°C} = -164\ kJ/mol \quad (45)$$
MeOH synthesis:
$$CO_2 + 3\ H_2 \rightarrow CH_3OH + H_2O \quad \Delta H_{25°C} = -49.5\ kJ/mol \quad (46)$$

The reaction selectivity is thus influenced by the reaction temperature, pressure, and the catalyst used. Additionally, the catalytic performance of Cu can be further improved by addition of promoters (e.g. Mn, Zr, Zn, Al)(47,48) and by various supports (e.g. graphitic carbon, $SiO_2$, CNT, MgO)(49–52). This can modulate active sites and the surface charge of Cu(53).

Studies have shown that the use of Pd, either alone or as a promoter of Cu, both over ZnO, can enhance selectivity towards various products of $CO_2$ hydrogenation(54,55). Siriworarat et al. (56) investigated the impact of Pd loading (5, 10, and 15 wt.%) on a Pd-Cu-Zn catalyst, where Cu and Zn comprised 25 wt.%. Conducted at 250 °C and 25 bar, the study demonstrated that the highest performance was achieved with the catalyst containing 15 wt.% Pd, 25 wt.% Cu, and 25 wt.% Zn, yielding MeOH space-time yield of 0.112 $kg_{MeOH}\ kg_{cat}^{-1}\ h^{-1}$. In another study by Díez-Ramírez et al., 37.5wt.% of Pd with CuZn/SiC exhibited the highest selectivity towards MeOH. In addition, Deerattrakul et al.(57) found that 15wt.% of CuZn(O) loading over a nitrogen-doped graphene aerogel achieved the highest MeOH production (0.095 $kg_{MeOH}\ kg_{cat}^{-1}\ h^{-1}$) at a reaction temperature of 250 °C and relatively low pressure of 15 bar. Collectively, the combination of Cu with Pd over ZnO or graphene as support may presents an intriguing avenue to enhance $CO_2$ hydrogenation to hydrocarbons, warranting further exploration through studies of monometallic Cu/ZnO, bimetallic CuPd/ZnO, or CuPd/Gr. Even more so, as one would rather avoid using nobel metals.

To add to the current understanding, different preparation protocols were adapted to prepare ZnO-supported CuPd (bimetallic) and graphene-supported CuPd, as well as ZnO supported Cu or Pd (monometallic) catalysts, as summarized in Table 1. The reduction temperature of the catalysts (monometallic) was varied (i.e., 200, 300, 500 °C) to investigate its influence on catalytic activity, catalyst morphology, particle size, and composition. High resolution transmission electron microscopy (HRTEM) with electron energy loss spectroscopy (EELS) and energy-dispersive X-ray spectroscopy (EDX), high-angle annular dark-field scanning transmission electron

microscopy (HAADF-STEM), and X-ray powder diffraction (XRD), were employed to analyze the size, distribution of metal particles, and the catalysts' composition. Furthermore, temperature-programmed reduction (TPR) provided insights into catalysts stability and metal-support interactions. Moreover, temperature-programmed desorption (TPD) revealed information about adsorption sites. On the reduced catalysts, the hydrogenation of $CO_2$ was carried out at atmospheric and elevated pressure of 20 bar in a continuous flow fixed-bed reactor, connected to a micro-gas chromatograph (GC) for kinetic measurements, with the reaction conducted at different temperatures. Selectivity and catalytic activity as a function of reaction temperature were compared for each catalyst.

Table 1. Catalysts examined in the current study (% refers to wt.%).

| Synthesized catalysts | Abbreviation |
|---|---|
| 5% CuPd (3:2) on ZnO or graphene (reduction method) | i. CuPd/ZnO-r  ii. CuPd/Gr-r |
| 5% CuPd (3:2) on ZnO (polyol synthesis method) | iii. CuPd/ZnO-p |
| 90% Cu- and Zn-nitrates reduced with $Na_2CO_3$ (co-precipitation method) | iv. 90Cu/ZnO-c |
| 5% Cu or Pd on ZnO (wet impregnation method) | v. Cu/ZnO-i  vi. Pd/ZnO-i |

## Results and discussion

### Catalysts synthesis and characterization

Figure 1A illustrates the synthesis procedures for obtaining different types of catalysts using supports of ZnO or graphene (Gr) (Table 1; for details see the *Experimental* section). Following a redox method (denoted by r)(58) for 5wt.% Cu/Pd (3:2), $H_2$-reduced Cu on ZnO or Gr were mixed with Pd salt under $N_2$ (Cu + $Pd^{2+}$ → $Cu^{2+}$ + Pd) forming (i) CuPd/ZnO-r or (ii) CuPd/Gr-r catalysts, respectively.

In a polyol synthesis(59,60), $Pd^{2+}$ and $Cu^{2+}$ ions were reduced by ethylene glycol and stabilized with 1-hexadecylamine as a ligand. The obtained CuPd alloy nanoparticles (NPs) were impregnated on the ZnO support forming (iii) CuPd/ZnO-p (p denotes polyol synthesis). Moreover, adopting a co-precipitation method(61), 90wt.% Cu and Zn nitrates were reduced together by aqueous $Na_2CO_3$, dried, and calcined at 350 °C to obtain (iv) 90Cu/ZnO-c catalyst (c denotes co-precipitation). (v) Cu/ZnO-i and (vi) Pd/ZnO-i were prepared by wet impregnation (denoted by i). In the following, for simplicity % loading refer to wt.%.

**ARTICLE**

In order to determine the morphology, elemental composition, and metal-support interactions of the prepared catalysts, HRTEM, EDX, and EELS mapping were employed. CuPd/ZnO-r was examined after $H_2$ pretreatment (Fig. 1B), and after $CO_2$ hydrogenation, as shown in Fig. 1C and Fig. S1. A notable aspect (EDX mapping in Fig. 1C) is the segregation of Cu and Pd within the NPs. Two potential reasons may account for CuPd/ZnO-r possessing a core-shell structure, formed during synthesis. As shown in Fig. 1A, CuPd/ZnO-r is formed through the direct deposition of Pd via a redox reaction, with Cu/ZnO already in place while Pd coats the Cu, resulting in the development of layered NPs. Second, the layered structure may arise from reaction conditions, as CO can displace (mobilize) Cu atoms (33,62) while the strong binding of CO to Pd drives its surface segregation. Given the layered morphology of the NP, the Cu:Pd ratio does not correspond to a specific phase. The line scan of a NP after CO hydrogenation (Fig. S2) confirmed that Cu is predominantly present in the core, while Pd is mainly located on the outer shell, which is also consistent with CuPd/ZnO-r observed after $CO_2$ hydrogenation (Fig. S1). Furthermore, the

of the ZnO support. Since there is no concurrent increase in oxygen within the particle, this suggests that Zn interacts with the particle, forming an interface alloy between particle and support.

The bimetallic CuPd/ZnO-p catalyst was examined both before (Fig. S3) and after $CO_2$ hydrogenation (Fig. S4). The EDX maps in Fig. S3 suggests that the NPs were CuPd alloys, with Fig. S4 showing a nearly uniform distribution of Cu and Pd within the NPs. No metallic Zn was detected in the NPs, although XRD detected PdZn alloys (see below).

A HRTEM image of the reduced CuPd/Gr-r catalyst is presented in Fig. 1D. By performing fast Fourier transformation (FFT) of a small image area encompassing the NP, the lattice distance was determined. This analysis was conducted for four different NPs, yielding the results listed in Table S1. The percentage of Cu was calculated using Vegard's rule, which assumes that an arbitrary mixture of two components (such as Cu and Pd) has the same face-centered cubic (fcc) crystal structure. Based on the lattice constant of Cu of 0.361 nm and
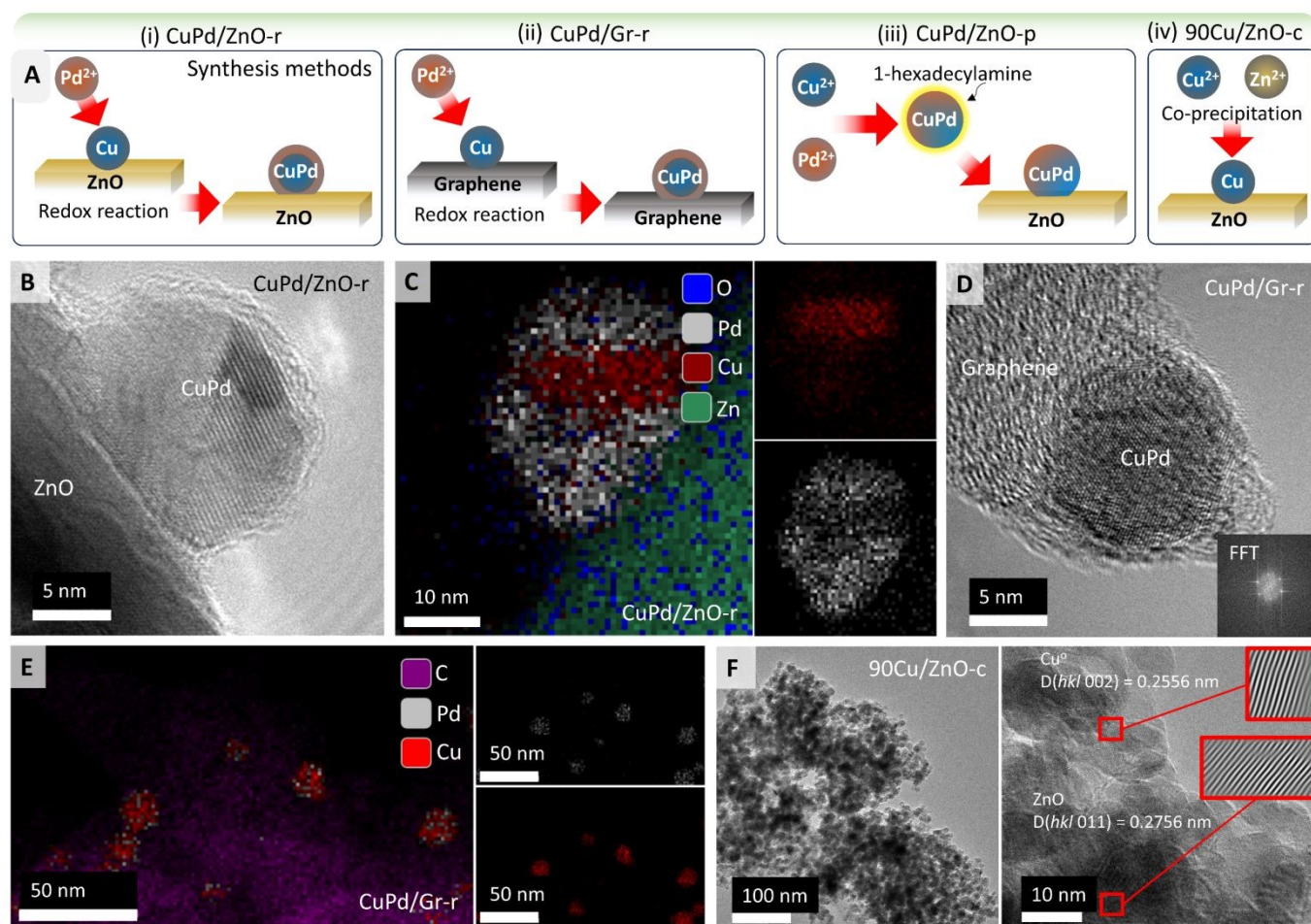


**Fig. 1. (A)** Schematics elaborating the synthesis of nanocatalysts through different methods, mainly (i) 5%Cu/Pd (3:2) over ZnO or (ii) graphene through liquid reduction method, (iii) Pd²⁺ and Cu²⁺ reduction by ethylene glycol, stabilization with 1-hexadecylamine and deposition on ZnO to obtain CuPd/ZnO-p, and (iv) 90% Cu with Zn nitrates, reduced with aqueous $Na_2CO_3$ to produce 90Cu/ZnO-c (for details of synthesis see the *Experimental* section) **(B)** HRTEM image of the bimetallic CuPd/ZnO-r catalysts **(C)** corresponding EDX mapping showing distribution of 'Pd', 'Cu' and 'O' atoms in CuPd/ZnO-r **(D)** HRTEM image of the CuPd/Gr-r catalysts **(E)** EDX mapping showing distribution of 'C', 'Pd', and 'Cu' atoms in CuPd/Gr-r **(F)** HRTEM image of the 90Cu/ZnO-c catalysts, also showing interplanar spacing of Cu (d = 0.256 nm) and ZnO (d = 0.277 nm).

concentration of Zn within the particle increases in the vicinity

that of Pd of 0.389 nm, successful incorporation of Cu into the Pd lattice can be assumed. Additionally, EDX analysis was applied for determining the elemental composition (Fig. 1E). EDX phase mapping clearly shows that the NPs mainly consist of Cu and Pd as assumed for Vegard's rule. The accompanying EDX plot (Fig. S5) shows the quantification spectra of the NPs, with results listed in Table S2. Similar to the results obtained via Vegard's rule, no discernible trend regarding NPs composition (Cu/Pd) ratio was observed.

In addition to EDX mapping, EDX line scans of the CuPd/Gr-r catalyst were acquired, depicted in Fig. S6. Notably, the NP in the central image exhibited a much lower Pd percentage than the other NPs. In the left image, an apparent increase in carbon content inside the NP was observed nearer to the support. Given that the inclusion of carbon inside the NPs is unlikely, the signal rather originates from the graphene-support under the NP. The line scan in the right image traverses two NPs, with Cu found between them, but no Pd. This suggests that sintering initiates by movement of Cu atoms (33) leading to coalescence on the graphene support.

The catalyst obtained via the co-precipitation method, with 90% Cu over ZnO (90Cu/ZnO-c), exhibited an average particle size of 12 nm (Fig. 1F), with NPs uniformly dispersed. The interplanar spacing of Cu was d = 0.256 nm, while for ZnO it was d = 0.277 nm. The lattice constant of fcc Cu is 0.361 nm, while ZnO exhibits a hexagonal crystal structure, with lattice parameters a = 0.32496 nm and c = 0.52042 nm. This confirms the assignment of the interplanar spacings and lattice structures to Cu and ZnO.

Similarly, the catalysts with low Cu or Pd loading (5%) over ZnO, obtained through a one pot wet-impregnation method, were also analyzed. The Cu/ZnO-i catalyst after reduction in $H_2$ showed a single Cu NP on ZnO (Fig. S7). Benefitting from the high resolution, lattice planes were analyzed for phase identification, i.e. in the red square an FFT was generated. After inverse FFT, the image revealed individual lattice planes without interference from background signals. The distance between lattice planes was measured to be 0.251 nm. Fig. S7 illustrates the unit cell of Cu, focusing on (1 1 0) lattice planes marked in purple, where the distance between two Cu atoms was measured as d(Cu-Cu) = 0.25 nm, as observed in the HRTEM image.

Additionally, Fig. S8 depicts a high-angle annular dark-field scanning transmission electron (HAADF-STEM) micrograph of the Pd/ZnO-i catalyst after $H_2$ reduction at 500 °C. Variations in intensity in HAADF images are attributed to differences in sample thickness or the atomic number. The red box surrounding the NP on the surface of the ZnO support (Fig. S8) was chosen for EDX analysis revealing reduced Pd and Zn, with an overall composition of 46.6 at% Pd and 53.4 at% Zn.

Figures S9 and S10 reveal the effect of high pressure (20 bar) and temperature (500 °C) on NP size in the course of the hydrogenation reaction. Bimetallic NPs (CuPd) showed significantly more sintering on graphene, increasing in size from 8.7 nm to 20 nm, than when supported by ZnO, for which NP size only increased from 8.4 nm to 11 nm. In contrast, monometallic NPs of both Cu and Pd on ZnO even exhibited a
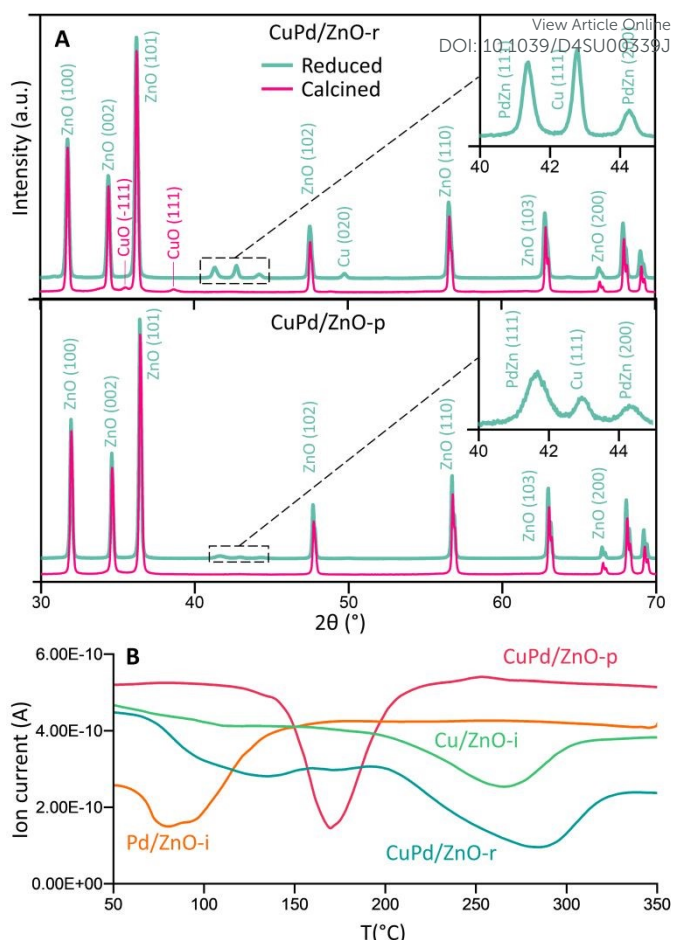
**Fig. 2. (A)** Crystal structure of calcined (500°C) and $H_2$-reduced CuPd/ZnO-r and CuPd/ZnO-p catalysts. The crystal structure of other catalysts can be seen in Fig. S9-S11 **(B)** $H_2$-temperature programme reduction (TPR) profile of calcined (500°C) CuPd/ZnO-r, CuPd/ZnO-p, Cu/ZnO-i and Pd/ZnO-i catalysts.

slight reduction in size, likely due to CO-induced redispersion (Fig. S9).

Fig. 2A and S11-S13 display (area-averaging) X-ray diffraction (XRD) patterns of the as-prepared (calcined) and $H_2$-reduced catalysts. For the CuPd/ZnO-r catalyst in the calcined state, CuO was identified, with no mixed CuPd oxide detected. Due to the small size of the metal particles, the Bragg peaks appear broader and blend into the background noise. Pd exhibits a higher affinity towards Zn, as a separate PdZn (1 1 1, 2 0 0) phase was detected after $H_2$ reduction at 500 °C, still with no signs of a CuPd alloy. This suggests that in CuPd/ZnO, Cu and Pd separate, also forming PdZn interfaces, in line with the locally-resolved HRTEM studies (see Fig. 1B). The CuPd/ZnO-p catalyst showed similar XRD patterns before and after $H_2$ reduction, with peaks related to PdZn being less intense than the ones for CuPd/ZnO-r. Conversely, the CuPd/Gr-r catalyst (Fig. S11) after $H_2$ reduction exhibited dominant diffraction from graphitic carbon (0 0 2), because of graphene calcination at elevated temperatures, in line with literature reports(63,64). Furthermore, the XRD patterns of the Cu/ZnO-i and Pd/ZnO-i catalysts (Fig. S12 and S13) after pretreatment in $H_2$ at different temperatures confirmed that PdO was reduced at 200 °C, while CuO reduction occurred at a higher temperature of 300 °C.

**ARTICLE**

Temperature-programmed reduction (TPR) studies were thus carried out to monitor the $H_2$-induced reduction behaviour of the (calcined) catalysts in more detail (10% $H_2$ in Ar). The mass spectrometer (MS) signals of $H_2$ (m/z = 2) were plotted against temperature, as shown in Fig. 2B and Fig. S14. Pd/ZnO-i exhibited $H_2$ consumption starting at a minimum temperature of 80°C, while Cu/ZnO-i was reduced at 270°C. In contrast, CuPd/ZnO-r and CuPd/ZnO-p displayed distinctly different profiles. For CuPd/ZnO-r, the minimum of Pd was slightly shifted to higher temperature (130°C), while the minimum for Cu was at 290°C. This again suggests that CuPd/ZnO-r consists of somewhat separate, but still connected Cu and Pd, likely within the NPs. The CuPd/ZnO-p profile exhibited only a single minimum at 170°C, indicating the presence of alloyed CuPd NPs.
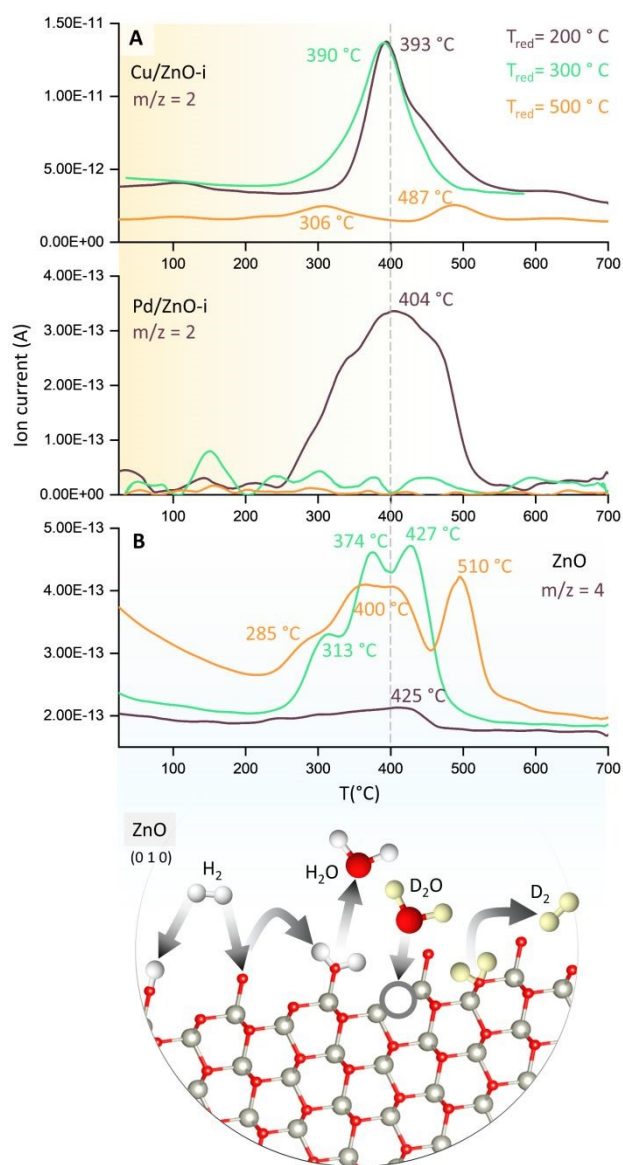


To evaluate the binding strength at and distribution of $H_2$

**Fig. 3.** Temperature programme desorption (TPD) studies of catalysts. **(A)** $H_2$-TPD of Cu/ZnO-i and Pd/ZnO-i for different reduction temperatures with m/z= 2 recorded, **(B)** $D_2$O-TPD of ZnO for different reduction temperatures with m/z= 4 recorded. Structure of ZnO with possible reaction pathways of $H_2$ and $D_2$(O) on the ZnO-surface (88).

adsorption sites, hydrogen-temperature programmed desorption ($H_2$-TPD) was performed, which also shed light on metal-support interactions. $H_2$-TPD was measured for both catalysts (Cu and Pd/ZnO-i) for each reduction temperature ($T_{200}$, $T_{300}$, and $T_{500°C}$). In Fig. 3A, the $H_2$ desorption profile of the Cu/ZnO-i catalysts revealed desorption maxima at 390 and 393°C for 200 and 300°C reduction temperatures, respectively. In contrast, the Cu/ZnO-i catalyst reduced at 500°C did not exhibit a clear desorption peak, potentially due to the high-temperature reduction process leading to the formation of a CuZn alloy or sintering, which weakens the chemical bonding of $H_2$ on the catalyst surface. Similarly, at higher reduction temperatures ($T_{300}$ and $T_{500°C}$), the Pd/ZnO-i catalysts did not display the desorption maximum observed after $T_{200°C}$ (Fig. 3A) anymore. This again suggests that Pd can rather easily form an alloy with Zn at temperatures exceeding 200 °C (65–67). Metallic Pd can absorb hydrogen into the NPs, which ceases upon forming a PdZn alloy. Analogously, previous studies with Pd-Pb alloys indicated a decreasing intensity of $H_2$ desorption upon addition of Pb (68). For calculation of the binding energy of molecules on the catalyst's surface, the Redhead approximation was applied (69). The energy of desorption ($E_{des}$) for Cu/ZnO-i was $E_{des}$ = 169 kJ/mol at $T_{max}$ = 390 °C, while for Pd/ZnO-i, it was $E_{des}$ = 174 kJ/mol at $T_{max}$ = 410 °C.

Furthermore, to detect surface defects in the ZnO support (70), TPD was performed with deuterium oxide ($D_2$O-TPD). The desorption behaviour of $D_2$ from $D_2$O adsorbed on the catalyst surface is indicative of the nature and density of surface defects or oxygen vacancies(71). Specifically, the desorption temperature and intensity of $D_2$ desorption peaks can reveal the availability and accessibility of surface defect sites. Higher desorption temperatures and/or broader desorption peaks may suggest stronger interactions between $D_2$O and defects, indicating vacancies in the ZnO support, which can influence the $CO_2$ and CO hydrogenation reaction(72).

In Fig. 3B, $D_2$ desorption from the ZnO surface is displayed. After catalyst reduction at 200°C and $D_2$O dosing, only weak $D_2$ desorption was observed. However, $D_2$ desorption peaks were clearly visible for reduction at 300 and 500°C, with peak maxima between 313 to 427 °C and 285 to 510 °C, respectively. A desorption peak at approximately 370°C is evident for every reduction temperature. Fig. 3B also illustrates potential processes involving the interaction of $H_2$ and $H_2$O, or $D_2$ and $D_2$O, with O vacancies on the ZnO surface. Due to the interaction of $D_2$O with surface defects of ZnO, oxygen vacancies can be re-filled and $D_2$ formed (m/z = 4). Literature also reported observations of surface defects in hydrothermally grown ZnO after exposure to $D_2$ gas at elevated temperatures(73).

## $CO_2$ and CO hydrogenation to methane or methanol

We then determined the $CO_2$ hydrogenation performance of the various catalysts (Fig. 4A) at 20 bar pressure and temperatures from 300 to 500°C, including CuPd/ZnO-r, CuPd/ZnO-p, CuPd/Gr-r, 90Cu/ZnO-c, Cu/ZnO-i, and Pd/ZnO-i. Prior to each measurement, the catalysts were reduced in

hydrogen flow. The reaction mixture consisted of 5% $CO_2$ and 20% $H_2$ in helium. $CO_2$ conversion increased with temperature, rising from about 5% at 300°C to >30% at 500°C. Notably, for the bimetallic catalysts, $CO_2$ conversion was at least 3% higher across all measured temperatures. CO and $CH_4$ were detected as main products of $CO_2$ hydrogenation, with the CO yield increasing linearly with temperature, reaching 20% at 500°C. Both for CuPd/ZnO-r and CuPd/ZnO-p, a significant increase was also observed in $CH_4$ yield (from 5.8% to 13%) as temperature increased from 350 to 400°C. At 500°C, CuPd/ZnO-r exhibited the highest $CH_4$ yield (16%) as compared to CuPd/ZnO-p and CuPd/Gr, which both yielded 14%. The monometallic Cu/ZnO-i had a $CH_4$ yield of 12%, while Pd/ZnO-i showed the lowest yield of 8%.

Very differently, the catalyst containing 90wt.% Cu (90Cu/ZnO-c), prepared by co-precipitation and tested at 230°C, exhibited selectivity towards MeOH rather than $CH_4$ (Fig. S15). Despite a $CO_2$ conversion of 5.5%, the MeOH yield remained constant over time, with little $CH_4$ detected. Overall, the CO yield was 4%, while MeOH was recorded at 2%. A similar trend had been observed in previous studies, demonstrating improved MeOH

selectivity/yield upon high Cu loading on ZnO(18,74) and observation of a volcano-like pattern in MeOH selectivity with respect to the Cu NPs size(75).

Furthermore, as RWGS may be followed by CO hydrogenation, the latter reaction was evaluated on Cu/ZnO-i, Pd/ZnO-i, and CuPd/ZnO-r under conditions similar to those of $CO_2$ hydrogenation, only 5% CO was used instead of $CO_2$ (Fig. 4B). Notably, from 400 to 500°C, CO conversion was at least 40% higher than $CO_2$ conversion. $CH_4$ (from methanation) and $CO_2$ (from WGS) were identified as the main products of CO hydrogenation, with the $CO_2$ yield increasing linearly with temperature, peaking 37% at 450°C and then dropping to 33% at 500°C. The $CH_4$ yield reached its highest level of 48% at 450°C and remained steady up to 500°C. No significant differences were observed between monometallic or bimetallic catalysts for CO hydrogenation. Nevertheless, ethane (from FT) was detected as a side product (≈4%) at 400°C (Fig. S16). Interestingly, the 90Cu/ZnO-c catalyst showed higher CO conversion of 14%, with a MeOH yield of 10% and $CO_2$ yield of 4.3% at 230°C (Fig. 4C). Overall, the MeOH yield remained constant at 8-10% over 300 minutes. This further confirmed
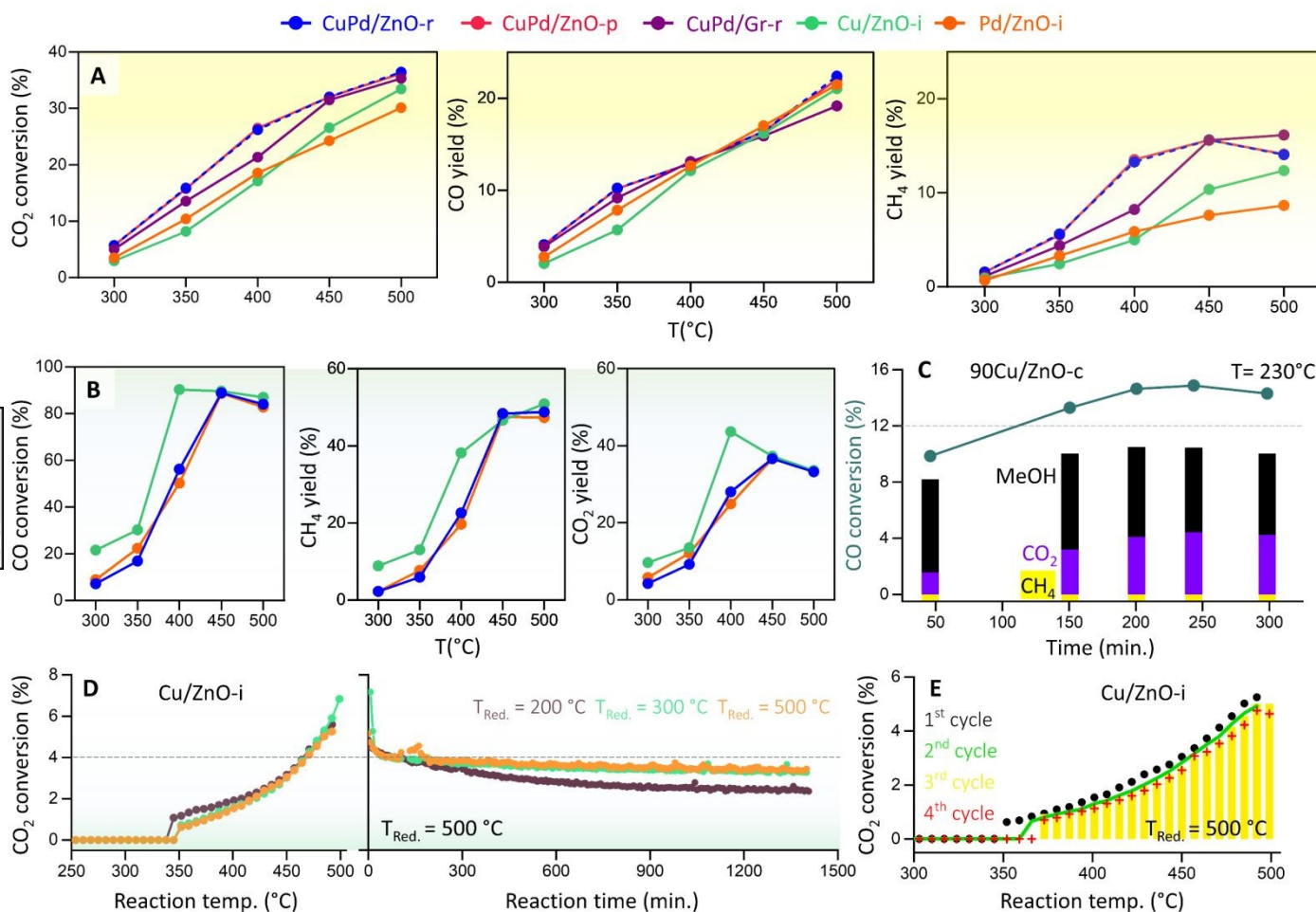


**Fig. 4.** Kinetic measurements of $CO_2$ and CO hydrogenation. **(A)** catalytic performance of CuPd/ZnO-r, CuPd/ZnO-p, CuPd/Gr-r, Cu/ZnO-i, and Pd/ZnO-i catalysts in terms of $CO_2$ conversion , CO and $CH_4$ yield at $p$ = 20 bar and T= 300-500°C, and **(B)** CO conversion, $CH_4$ and $CO_2$ yield by CuPd/ZnO-r, Cu/ZnO-i, and Pd/ZnO-i at $p$ = 20 bar and T= 300-500°C **(C)** CO hydrogenation to MeOH (%) and $CO_2$ (%) by 90Cu/ZnO-c catalysts at $p$ = 20 bar and T= 230°C (for $CO_2$ hydrogenation, see Fig. S15) **(D)** $CO_2$ conversion(%) to CO by Cu/ZnO-i catalysts reduced at different temperatures, at $p$ = 1 bar and T= 300-500°C, "reaction time" refers to the time on stream under constant conditions (for Pd/ZnO-i catalyst, see Fig. S17), and **(E)** $CO_2$ conversion (%) to CO over multiple cycles (for the Cu/ZnO-i catalyst reduced at 500°C).

**ARTICLE**

that a $CO/H_2$ gas feed increases the MeOH yield $(CO+2H_2\rightarrow CH_3OH)$(17,41). Indeed, for best performance, a mixture of $CO_2/CO/H_2$ (5%/20%/75%) is known to be required (76).The conducted experiments confirm that the hydrogenation of CO yields more $CH_4$ or MeOH than $CO_2$ hydrogenation. Thus, for MeOH production at industrial level using Cu/ZnO-based catalysts, CO serves as the major feed gas (20%) alongside $CO_2$ and $H_2$ (11).

The catalytic performance of the best performing catalysts was further described by calculating the space-time yield (STY) (more details in supplementary information) which includes the amount of the catalyst (0.1 g) used during the reaction:

- For $CO_2$ hydrogenation to $CH_3OH$ over 90Cu/ZnO-c, STY was 0.0836 $g_{MeOH}\cdot g_{cat}^{-1}\cdot h^{-1}$, and for CO hydrogenation, its STY was 0.4811 $g_{MeOH}\cdot g_{cat}^{-1}\cdot h^{-1}$.
- For $CO_2$ hydrogenation to $CH_4$, CuPd/Gr-r showed best performance with STY of 0.2416$g_{CH_4}\cdot g_{cat}^{-1}\cdot h^{-1}$, while for CO hydrogenation, Cu-ZnO-i exhibited the best STY of 0.7618 $g_{CH_4}\cdot g_{cat}^{-1}\cdot h^{-1}$.

A CuO/ZnO catalyst obtained through an ammonia-evaporation-induced synthetic method involving impregnation of filament-like ZnO for $CO_2$ hydrogenation at 3 bars showed the best performance, with a MeOH STY of 0.55 $g_{MeOH}\cdot g_{cat}^{-1}\cdot h^{-1}$ and a selectivity of 78.2%(77). Moreover, Han *et al.*(78) observed that doping Cu/ZnO catalysts with Pd, Pt, and Ru led to the formation of electron-rich Cu sites due to partial electron transfer, greatly enhancing $CO_2$ activation. The Pd-doped catalyst demonstrated the highest MeOH STY of 0.52 $g_{MeOH}\cdot g_{cat}^{-1}\cdot h^{-1}$ with 100-hour stability. In contrast, over a $Cu_{0.5}Ni_{0.5}/\gamma-Al_2O_3$ catalyst at 5 bar pressure, Reddy *et al.*(79) reported $CO_2$ conversion not exceeding 30% to CO. During the reaction, the Cu core atoms migrated toward the surface, resulting in the restructuring of the Cu@Ni core–shell structure to a Cu–Ni alloy, which functioned as the active site by enhancing CO desorption.

To examine the effect of pressure, $CO_2$ hydrogenation was also studied at atmospheric pressure (1 bar) from 250 to 500°C, using Cu/ZnO-i or Pd/ZnO-i catalysts, pre-reduced at different temperatures ($T_{red}$= 200, 300, and 500°C) (Fig. 4D). CO was the primary product of both catalysts. The $CO_2$ conversion of Pd/ZnO-i was 11% higher than the one of Cu/ZnO-i for every reduction temperature. A reaction temperature of about 300°C was necessary for CO formation with the Pd/ZnO-i catalyst, whereas with Cu/ZnO-i amounts of CO were first detected at 380°C. According to literature (80–83), the reaction mechanism involves the adsorption of $CO_2$ on the ZnO-supported Cu or Pd catalysts, leading to intermediate-carbonate formation.

To evaluate the catalysts' stability, a 24-hour reaction was carried out at 500°C. Each catalyst underwent reduction pretreatment at 200, 300, or 500°C before the long-term reaction. The Cu/ZnO-i catalyst reduced at 200°C exhibited more pronounced deactivation than those pre-reduced at 300 or 500°C (Fig. 4D). It appears that reduction at 200°C was insufficient, with CuO still being present. During the reaction, the partly reduced sample was subjected to 500°C and a gas flow of 20 vol% $H_2$, then leading to sintering of remaining CuO

NPs and final reduction to metallic Cu. The Cu/ZnO-i catalysts reduced at 300 and 500°C displayed almost constant $CO_2$ conversion to CO over the 24-hour reaction period (Fig. 4D). In contrast, the Pd/ZnO-i catalyst exhibited some $CO_2$ conversion to CO at 200°C, possibly due to metallic Pd already being present on the catalyst surface at this reduction temperature (Fig. S15). The increase in reduction temperature resulted in surface alloy formation(55,84), as indicated by the presence of a PdZn alloy in XRD (Fig. S11). Additionally, cyclic and long-term reactions demonstrated the stability of both catalysts, with no signs of decreasing $CO_2$ conversion observed over multiple reaction cycles or for lower reduction temperatures (Fig. 4E and Fig. S17).

For MeOH production over Cu/ZnO catalysts, a formate pathway has been proposed in the literature(85). A DFT study by Grabow and Mavrikakis(86) demonstrated that $CO_2$ hydrogenation over Cu/ZnO occurs via the formate pathway ($CO_2^* \rightarrow HCOO^* \rightarrow HCOOH^* \rightarrow CH_3O_2^* \rightarrow CH_2O^* \rightarrow CH_3O^* \rightarrow CH_3OH^*$). Meanwhile, MeOH production from CO follows the sequence $CO^* \rightarrow HCO^* \rightarrow CH_2O^* \rightarrow CH_3O^* \rightarrow CH_3OH^*$. Nevertheless, it is well documented in the literature that methanation, particularly over Pd-based bimetallic catalysts (e.g., CuPd), can follow either the formate or reverse-water gas shift (RWGS) pathways(87). Future studies employing *in situ* or *operando* techniques may provide confirmation of these intermediates, although the mechanism is still controversially discussed (83).

## Conclusions

Not unexpectedly, hydrogenation of $CO_2$ or CO to $CH_4$ and/or MeOH by catalysts of Cu, Pd, and PdCu NPs supported on ZnO or graphene has shown promise for reducing $CO_2$ emissions. Through a comprehensive characterization involving various techniques such as HRTEM, EDX, HAADF-STEM, XRD, $H_2$-TPR and -TPD, $D_2O$-TPD, as well as $CO_2$/CO hydrogenation kinetics, it was observed that lower Cu or Pd loadings (5%) supported on ZnO or graphene favored $CH_4$ production from 300 to 500°C and 20 bar pressure. CO was the major byproduct, indicating the occurrence of the reverse water gas shift (RWGS) reaction. The addition of the noble metal Pd to Cu had only minor effect on performance. In contrast, higher Cu content (90%) strongly increased MeOH production both in $CO_2$ and CO hydrogenation at high pressure (20 bar).

$CO_2$ hydrogenation at ambient pressure (1 bar) and high temperature (300-500°C) on both Cu and Pd on ZnO produced CO as major product, corroborating that high pressure is inevitable for $CH_4$/MeOH production.

For CO hydrogenation at 400 to 500°C, CO conversion was at least 40% higher than that of $CO_2$ conversion, with $CH_4$ and $CO_2$ identified as the main products. Again, utilizing 90% Cu supported on ZnO led to enhanced CO conversion of 14%, with a MeOH yield reaching 10% and a $CO_2$ yield reaching 4.3% at 230°C.

The findings underline the significance of catalyst (NP) composition, affected by the corresponding synthesis

methodologies, for optimizing $CO_2$ and CO hydrogenation processes for efficient methane or methanol production. This offers useful insights for advancing sustainable energy solutions.

## Experimental

### Catalysts synthesis

The bimetallic catalysts were synthesized employing two distinct methods. For the first method (Fig. 1A), Cu was initially deposited on the support, followed by the addition of palladium salt to initiate a redox reaction and form alloyed NPs. The synthesis was conducted on both ZnO powder and graphene, with a total metal loading of 5wt.% and a Pd/Cu ratio of 2:3. Copper acetate monohydrate (0.19 g) was dissolved in distilled water under stirring, followed by the addition of 1.90 g ZnO (or graphene nanoplatelets), and the suspension was stirred overnight. The mixture was then heated to 130°C to evaporate the water, and the solid was dried for 2 hours at 120°C. Subsequently, the catalyst was calcined at 500 °C for 2 hours in air, and then reduced with $H_2$ at 350 °C for 2 hours. In a separate step, a solution of palladium acetate in water was prepared, and the reduced copper catalyst was added to the solution under a flow of nitrogen. After evaporating the water and drying, the catalyst was calcined at 500 °C for 2 hours before reduction in the reactor prior to kinetic measurements. The prepared catalysts are named "CuPd/ZnO-r" and "CuPd/Gr-r".

In the second method (Fig. 1A), 1-hexadecylamine (HDA) capped Pd-Cu nanoparticles were synthesized and then dissolved in toluene for impregnation on ZnO. The metal loading was 5wt.%, with a Pd:Cu ratio of 2:3. In a round-bottom flask equipped with a magnetic stirrer, refluxing device, and nitrogen purging source, 80 ml of ethylene glycol was cooled with an ice bath and degassed for ten minutes under a stream of nitrogen. Copper acetate hydrate (0.95 g) and palladium acetate (0.43 g) were added to the flask, followed by the addition of 4.8 g of HDA to the ethylene glycol solution kept in the ice bath. The mixture was heated to 60 °C until HDA dissolved, resulting in a color change from blue to green. The solution was then heated to 160 °C and maintained at this temperature overnight. The color of the solution changed from deep blue/violet to green, then blue, and finally black, with a red layer, likely $Cu_2O$, deposited on the inner wall of the flask. After cooling to room temperature, the black NPs were separated by centrifugation and washed three times with ethanol to remove excess HDA and ethylene glycol. The NPs were dried overnight, resulting in a yield of approximately 58.7%. Subsequently, the nanoparticles were deposited on ZnO. The required amount of NPs for a metal loading of 5wt.% was calculated, and 0.1 g of NPs was suspended in toluene with 1.89 g of ZnO. After removing all toluene under vigorous stirring at about 150°C, the precipitate was dried overnight at 125°C, followed by calcination in air at 500°C for 2 hours to completely remove HDA. The reduction of metal oxides was performed in the reactor before conducting kinetic measurements. The resulting catalyst weighed 1.77 g, representing a yield of 88.5%, named "CuPd/ZnO-p".

Using a co-precipitation method(61) copper nitrate (90%) and Zn nitrates (10%) were reduced with aqueous $Na_2CO_3$, dried, and calcined at 350°C to obtain the "90Cu/ZnO-c" catalyst (Fig. 1A).

The monometallic Cu and Pd catalysts were prepared via the wet-impregnation ("-i") method of a ZnO support. Each catalyst was synthesized by weighing 0.32 g of copper acetate monohydrate or 0.21 g of palladium acetate. The metal salt was then suspended in 30 mL toluene in a flask, ensuring complete dissolution by adding a few drops of ethanol. Subsequently, 1.90 g of ZnO powder was added, and the suspension was stirred overnight at room temperature. The solvent was evaporated by heating the mixture to 150°C, and the resulting solid was dried for 2 hours in an oven at 120°C. Calcination of the catalysts was performed in air at 500°C for 2 hours, using a heating rate of 10°C/min. This calcination step was essential for removing the acetate from the catalyst and converting the metals into oxides. Prior to kinetic measurements, the catalysts underwent reduction in the reactor. The reduction was carried out using a 10 vol% hydrogen/He flow at three different temperatures: 200°C, 300°C, and 500°C. The prepared catalysts were named "Cu/ZnO-i" and "Pd/ZnO-i".

### Catalysts characterization

The morphology and crystal structure of the catalysts were analyzed using a FEI TECNAI G2 F20™ at the University Service Center for Transmission Electron Microscopy (USTEM) at TU Wien. The microscope was equipped with a field emission gun (X-FEG) operated at an acceleration voltage of 200 kV. Additionally, an energy dispersive X-Ray (EDX) silicon drift detector (SSD) (EDAX Apollo XLT SSD™) was incorporated into the TEM. Catalyst samples were loaded onto a carbon-coated Cu grid and then inserted into the TEM's inlet system using a single tilt holder. Various TEM images, including high-angle annular dark field (HAADF), and high-resolution (HR) TEM images, were recorded for each catalyst both before and after reaction. Structural alterations during the reaction were discerned through image comparison, with the high resolution of HRTEM images allowing for precise measurement of lattice planes to identify different phases. Additionally, energy dispersive X-ray spectroscopy (EDX) and electron energy loss spectroscopy (EELS) measurements were conducted to investigate alloy formation. Particle size and distribution were analyzed using DigitalMicrograph software (Gatan™).

The XRD measurements were primarily carried out to elucidate the atomic structure of various crystalline phases (metals, alloys, oxides). Diffractograms were acquired using a PANanalytical X´Pert Pro™ Bragg-Brentano™ powder diffractometer at the X-ray Center of TU Wien. Cu K-α with a wavelength of 1.54 Å served as the radiation source. A small amount of each catalyst (including calcined catalysts and those subjected to three different reduction temperatures) was applied to a silicon wafer (Si (7 1 1 1) layer) fixed to a sample holder. The position (2θ angle) of the measured reflexes was compared with diffractograms from a database (COD Crystallography Open Database™) to identify crystalline phases.

RSC Sustainability

Rietveld refinement was employed to quantify the different compounds present in the diffractograms. This technique utilizes the least squares method to fit a theoretical line profile to the observed reflexes until a satisfactory match is achieved. Furthermore, Rietveld refinement facilitated the calculation of the crystallite size of both the support and the metal particles (using HighScore Plus 4.1 – PANalytical software™).

Temperature programmed reduction (TPR) served as a standard method for gathering insights into the reducibility of a material. The $H_2$ TPR analysis was conducted in a continuous fixed bed quartz tube reactor. Approximately 50 mg of catalyst was loaded into the reactor tube, which was then positioned in a heating furnace. Gas flows of Argon and $H_2$ (the reducing gas) were carefully regulated using calibrated mass flow controllers. A total flow of 100 mL min$^{-1}$ with 10 vol% $H_2$ in Ar was passed through the sample. During the experiment, the furnace underwent heating from room temperature to 500°C at a rate of 10°C min$^{-1}$. The quartz tube reactor was linked to a quadrupole mass spectrometer (Balzers Prisma™), which recorded the mass signals of $H_2$ (m/z = 2) and $H_2O$ (m/z = 18) over time as a function of temperature. These experiments were carried out for both synthesized catalysts and the pure ZnO support.

Temperature programmed desorption (TPD) provided insights into the binding energy of absorbed molecules. The experiments were conducted within a solid quartz tube reactor in a conjunction with a quadrupole mass spectrometer (Balzers Prisma™). Each catalyst, weighing 50 mg, was fixed with quartz wool and loaded into the reactor tube. To facilitate the adsorption of gas molecules on the surface, the catalyst was exposed to a gas mixture containing probe molecules such as $H_2$ or $D_2O$ (100 or 10 mbar gas pressure, respectively). The Redhead approximation (Eq.1) (69) can be applied for calculating the binding energy of molecules on the catalyst's surface:

$$E_{des} = R * T_{max} * \left[\ln\left(\frac{v*T_{max}}{\beta}\right) - 3,46\right] \dots\dots \text{ (Eq.1)}$$

| | |
|---|---|
| $E_{des}$ | Activation energy of desorption |
| $T_{max}$ | Temperature at peak maximum |
| $\beta$ | Heating rate (dT/dt) |
| n | Order of desorption |
| v | Frequency factor |

In general, the Redhead-equation is valid for first-order desorption (single step desorption). As approximation, Eq.1 was used with a frequency factor of v = 10$^{13}$ s$^{-1}$.

Moreover, $D_2O$ TPD of ZnO was carried out after reduction at various temperatures, and m/z = 4 signals were recorded. This experiment provided insights into possible vacancies within the support. Due to the interaction of $D_2O$ with surface defects of ZnO, $D_2$ was formed and detected by the mass spectrometer (m/z = 4). The same preparation and measurement steps as those used for $H_2$ TPD were applied, with a partial pressure of 10 mbar $D_2O$ utilized for adsorption.

## CO$_2$ and CO hydrogenation

The kinetic measurements were conducted in PID, Eng&Tech Microactivity Effi Reactor™, a 30 cm long stainless-steel tubular reactor with an internal diameter of 9.91 mm, in a temperature range of 25 to 800 °C and pressures up to 20 bar. Feed gases including $H_2$, $O_2$, CO, $CO_2$, and He were introduced into the reactor, with flow rates regulated by calibrated mass flow controllers. Online product analysis was performed via a micro-GC system (Inficon™; 300 Micro GC, runtime < 2 min), equipped with a molecular sieve, a plotQ column™ and a Thermal Conductivity Detector (TCD). The molecular sieve effectively separated small molecules such as $H_2$, $O_2$, and $N_2$, while the plotQ column facilitated the separation of carbon-containing compounds. Kinetic measurements were conducted for $CO_2$ and CO hydrogenation at 20 bar (or ambient pressure) and various temperatures ranging from 230 to 500 °C. Each temperature step was held constant for 8 hours, with average values taken for further calculations. This duration allowed the catalyst to reach a quasi-stationary state, minimizing the effects of transient behaviour. The total gas flow was maintained at 10 ml/min (corresponding to a flow of $6.81 \times 10^{-6}$ mol/s), comprising 5 % $CO_2$ or CO and 20 % $H_2$ in helium. Following each reaction period at a specific temperature, a reactivation treatment was applied. For this, the catalyst underwent oxidation with 10 % $O_2$ in He at 500 °C to remove carbonaceous deposits, followed by reduction with 10 % $H_2$ in He.

The TCD was calibrated prior to the experiments using standard gas mixtures to ensure accurate quantification of the detected species. Calibration curves were generated by plotting the peak areas against the known concentrations of the standards ($CO_2$, CO, and $H_2$ respectively). Linear regression was used to determine the relationship between peak area and concentration. During the experiments, the peak areas corresponding to the different reactants and products were recorded. These peak areas were then used to determine the concentrations of the molecules present. The calibrated peak areas from GC chromatograms were then utilized for calculation of the, e.g., $Conversion_{CO_2}(\%)$ in Eq.2,

$$Conversion_{CO_2}(\%) = \frac{A_{CO_2}^{in} - A_{CO_2}^{out}}{A_{CO_2}^{in}} \; 100 \dots\dots \text{ (Eq.2)}$$

with

$A_{CO_2}^{in}$ = Peak Area of $CO_2$ entering the reactor

$A_{CO_2}^{out}$ = Peak Area of $CO_2$ exiting the reactor

Analogously, for CO hydrogenation the CO GC peak areas were utilized for calculation of the CO conversion.

The selectivity of the catalysts for producing MeOH $Selectivity_{MeOH}(\%)$ was determined using Eq.3,

$$Selectivity_{MeOH}(\%) = \frac{A_{MeOH}}{A_{MeOH} + A_{CH_4} + A_{CO_2}} \cdot 100 \dots\dots \text{ (Eq.3)}$$

with

$A_{MeOH}$ = Peak area of MeOH

RSC Sustainability Accepted Manuscript

$A_{CH_4}$ = Peak area of CH$_4$

$A_{CO_2}$ = Peak area of CO$_2$

Similarly, the CH$_4$ $Selectivity_{CH_4}(\%)$ was determined using Eq.4

$$Selectivity_{CH_4}(\%) = \frac{A_{CH_4}}{A_{CH_4} + A_{MeOH} + A_{CO_2}} \cdot 100 ...... (Eq.4)$$

With conversion (Eq. 2) and selectivity (Eq. 3 or 4), the yield of MeOH, CH$_4$, or CO can be calculated using Eq. (5), (6), and (7),

$$Yield_{MeOH}(\%) = \frac{Conversion_{CO_2} \times Selectivity_{MeOH}}{100} ....... (Eq. 5)$$

$$Yield_{CH_4}(\%) = \frac{Conversion_{CO_2} \times Selectivity_{CH_4}}{100} ....... (Eq. 6)$$

$$Yield_{CO}(\%) = \frac{Conversion_{CO_2} \times Selectivity_{CO}}{100} ....... (Eq. 7)$$

For CO hydrogenation, yields were calculated analogously.

For the Gas Hourly Space Velocity (GHSV), Residence Time (τ), and Space Time Yield (STY) calculation, refer to supplementary note 1 of the electronic supplementary information.

## Data availability statement

The data supporting this article have been included as part of the Supplementary Information.

## CRediT Authorship Contribution Statement

*QM*: Conceptualization, Methodology, Validation, Software, Formal analysis, Investigation, Data curation, Writing – original draft, Writing – review & editing. *KD*: Conceptualization, Methodology, Validation, Formal analysis, JS, Data curation, Writing – review & editing. *MH*: Methodology, Validation, Formal analysis, Investigation, Writing – review & editing. *KLK, TS, SL, AA, and JN*: Formal analysis, Data curation, Validation, Writing – review & editing. *GR*: Conceptualization, Validation, Resources, Writing – review & editing, Supervision.

## Conflicts of interest

There are no conflicts of interest to declare.

## Acknowledgements

## Electronic Supplementary Information (ESI)

Following ESI is available online (DOI:xxxxxx)
- Figs. S1 to S17
- Table S1 to S2
- Supplementary note 1

## Notes and references

1.  Yoro KO, Daramola MO. CO2 emission sources, greenhouse gases, and the global warming effect. Adv Carbon Capture Methods, Technol Appl. 2020 Jan 1;3–28.

2.  Global Monitoring Laboratory - Carbon Cycle Greenhouse Gases [Internet]. [cited 2024 Apr 20]. Available from: https://gml.noaa.gov/ccgg/trends/

3.  Bhatt H, Davawala M, Joshi T, Shah M, Unnarkat A. Forecasting and mitigation of global environmental carbon dioxide emission using machine learning techniques. Clean Chem Eng [Internet]. 2023;5:100095. Available from: https://www.sciencedirect.com/science/article/pii/S277278 2823000037

4.  Carbon Capture, Utilisation and Storage - Energy System - IEA [Internet]. [cited 2024 Apr 20]. Available from: https://www.iea.org/energy-system/carbon-capture-utilisation-and-storage

5.  Net Zero Emissions by 2050 Scenario (NZE) – Global Energy and Climate Model – Analysis - IEA [Internet]. [cited 2024 Apr 20]. Available from: https://www.iea.org/reports/global-energy-and-climate-model/net-zero-emissions-by-2050-scenario-nze

6.  Zhang Q, Liu J, Wang G, Gao Z. A new optimization model for carbon capture utilization and storage (CCUS) layout based on high-resolution geological variability. Appl Energy. 2024 Jun 1;363:123065.

7.  Deerattrakul V, Yigit N, Rupprechter G, Kongkachuichay P. The roles of nitrogen species on graphene aerogel supported Cu-Zn as efficient catalysts for CO2 hydrogenation to methanol. Appl Catal A Gen. 2019 Jun 25;580:46–52.

8.  Díez-Ramírez J, Dorado F, De La Osa AR, Valverde JL, Sánchez P. Hydrogenation of CO2to Methanol at Atmospheric Pressure over Cu/ZnO Catalysts: Influence of the Calcination, Reduction, and Metal Loading. Ind Eng Chem Res. 2017;56(8):1979–87.

9.  Behrens M, Ehrens MB. Promoting the Synthesis of Methanol: Understanding the Requirements for an Industrial Catalyst for the Conversion of CO2. Angew Chemie Int Ed [Internet]. 2016 Nov 21 [cited 2024 Jun 28];55(48):14906–8. Available from: https://onlinelibrary.wiley.com/doi/full/10.1002/anie.2016 07600

10. Numpilai T, Chanlek N, Poo-Arporn Y, Wannapaiboon S, Cheng CK, Siri-Nguan N, et al. Pore size effects on physicochemical properties of Fe-Co/K-Al2O3 catalysts and their catalytic activity in CO2 hydrogenation to light olefins.

Appl Surf Sci. 2019 Jul 31;483:581–92.

11. Behrens M, Studt F, Kasatkin I, Kühl S, Hävecker M, Abild-Pedersen F, et al. The Active Site of Methanol Synthesis over Cu/ZnO/Al₂O₃ Industrial Catalysts. Science (80- ) [Internet]. 2012;336(6083):893–7. Available from: https://www.science.org/doi/abs/10.1126/science.1219831

12. Grunwaldt JD, Molenbroek AM, Topsøe NY, Topsøe H, Clausen BS. In Situ Investigations of Structural Changes in Cu/ZnO Catalysts. J Catal. 2000 Sep 10;194(2):452–60.

13. Van Den Berg R, Prieto G, Korpershoek G, Van Der Wal LI, Van Bunningen AJ, Lægsgaard-Jørgensen S, et al. Structure sensitivity of Cu and CuZn catalysts relevant to industrial methanol synthesis. Nat Commun 2016 71 [Internet]. 2016 Oct 5 [cited 2024 Apr 23];7(1):1–7. Available from: https://www.nature.com/articles/ncomms13057

14. Kuld S, Thorhauge M, Falsig H, Elkjær CF, Helveg S, Chorkendorff I, et al. Quantifying the promotion of Cu catalysts by ZnO for methanol synthesis. Science (80- ) [Internet]. 2016 May 20 [cited 2024 Jun 28];352(6288):969–74. Available from: https://www.science.org/doi/10.1126/science.aaf0718

15. Divins NJ, Kordus D, Timoshenko J, Sinev I, Zegkinoglou I, Bergmann A, et al. Operando high-pressure investigation of size-controlled CuZn catalysts for the methanol synthesis reaction. Nat Commun 2021 121 [Internet]. 2021 Mar 4 [cited 2024 Mar 4];12(1):1–10. Available from: https://www.nature.com/articles/s41467-021-21604-7

16. Dasireddy VDBC, Likozar B. The role of copper oxidation state in Cu/ZnO/Al2O3 catalysts in CO2 hydrogenation and methanol productivity. Renew Energy. 2019 Sep 1;140:452–60.

17. Zhang Z, Chen X, Kang J, Yu Z, Tian J, Gong Z, et al. The active sites of Cu–ZnO catalysts for water gas shift and CO hydrogenation reactions. Nat Commun 2021 121 [Internet]. 2021 Jul 15 [cited 2024 Mar 4];12(1):1–9. Available from: https://www.nature.com/articles/s41467-021-24621-8

18. Xie G, Jin R, Ren P, Fang Y, Zhang R, Wang Z jun. Boosting CO2 hydrogenation to methanol by adding trace amount of Au into Cu/ZnO catalysts. Appl Catal B Environ. 2023 May 5;324:122233.

19. Laudenschleger D, Ruland H, Muhler M. Identifying the nature of the active sites in methanol synthesis over Cu/ZnO/Al2O3 catalysts. Nat Commun 2020 111 [Internet]. 2020 Aug 4 [cited 2024 Mar 4];11(1):1–10. Available from: https://www.nature.com/articles/s41467-020-17631-5

20. Tóth M, Kiss J, Oszkó A, Pótári G, László B, Erdohelyi A. Hydrogenation of carbon dioxide on Rh, Au and Au-Rh bimetallic clusters supported on titanate nanotubes, nanowires and TiO 2. Top Catal [Internet]. 2012 Aug 25 [cited 2024 Jul 21];55(11–13):747–56. Available from: https://link.springer.com/article/10.1007/s11244-012-9862-7

21. Yu M, Sui PF, Fu XZ, Luo JL, Liu S, Yu M, et al. Specific Metal Nanostructures toward Electrochemical CO2 Reduction: Recent Advances and Perspectives. Adv Energy Mater [Internet]. 2023 Jan 1 [cited 2024 Apr 23];13(2):2203191.

Available from: https://onlinelibrary.wiley.com/doi/full/10.1002/aenm.202203191

22. Rabl H, Myakala SN, Rath J, Fickl B, Schubert JS, Apaydin DH, et al. Microwave-assisted synthesis of metal-organic chalcogenolate assemblies as electrocatalysts for syngas production. Commun Chem 2023 61 [Internet]. 2023 Mar 1 [cited 2024 Jun 10];6(1):1–8. Available from: https://www.nature.com/articles/s42004-023-00843-3

23. Hong J, Zhang W, Ren J, Xu R. Photocatalytic reduction of CO 2 : a brief review on product analysis and systematic methods. Anal Methods [Internet]. 2013 Feb 14 [cited 2024 Apr 23];5(5):1086–97. Available from: https://pubs.rsc.org/en/content/articlehtml/2013/ay/c2ay26270c

24. Cui Y, Labidi A, Liang X, Huang X, Wang J, Li X, et al. Pivotal Impact Factors in Photocatalytic Reduction of CO2 to Value-Added C1 and C2 Products. ChemSusChem [Internet]. 2024 [cited 2024 Jun 19];e202400551. Available from: https://onlinelibrary.wiley.com/doi/full/10.1002/cssc.202400551

25. Naghdi S, Cherevan A, Giesriegl A, Guillet-Nicolas R, Biswas S, Gupta T, et al. Selective ligand removal to improve accessibility of active sites in hierarchical MOFs for heterogeneous photocatalysis. Nat Commun 2022 131 [Internet]. 2022 Jan 12 [cited 2024 Jun 19];13(1):1–12. Available from: https://www.nature.com/articles/s41467-021-27775-7

26. Kisch H, Bahnemann D. Best Practice in Photocatalysis: Comparing Rates or Apparent Quantum Yields? J Phys Chem Lett [Internet]. 2015 May 21 [cited 2024 Jun 24];6(10):1907–10. Available from: https://pubs.acs.org/doi/full/10.1021/acs.jpclett.5b00521

27. Zhou W, Brack E, Ehinger C, Paterson J, Southouse J, Copéret C. Reactivity Switch of Platinum with Gallium: From Reverse Water Gas Shift to Methanol Synthesis. J Am Chem Soc [Internet]. 2024 [cited 2024 Apr 22];146:10806–11. Available from: https://pubs.acs.org/doi/full/10.1021/jacs.4c01144

28. Kampe P, Herrmann N, Wesner A, Ruhmlieb C, Albert J. Catalyst and Parameter Optimization Study for Slurry-Phase Methanol Synthesis Using Ni-Doped Indium-Based Catalysts. ACS Sustain Chem Eng [Internet]. 2023 Oct 2 [cited 2024 Apr 22];11(39):14633–44. Available from: https://pubs.acs.org/doi/full/10.1021/acssuschemeng.3c05584

29. Jia X, Sun K, Wang J, Shen C, Liu C jun. Selective hydrogenation of CO2 to methanol over Ni/In2O3 catalyst. J Energy Chem. 2020 Nov 1;50:409–15.

30. Wu C, Lin L, Liu J, Zhang J, Zhang F, Zhou T, et al. Inverse ZrO2/Cu as a highly efficient methanol synthesis catalyst from CO2 hydrogenation. Nat Commun 2020 111 [Internet]. 2020 Nov 13 [cited 2024 Apr 22];11(1):1–10. Available from: https://www.nature.com/articles/s41467-020-19634-8

31. Meng M, Li J, Zou H, Zheng J, Wu TAS, Chan TIS, et al. Methanol Synthesis at a Wide Range of H2/CO2 Ratios over

a Rh-In Bimetallic Catalyst. Angew Chemie [Internet]. 2020 Sep 7 [cited 2024 Apr 22];132(37):16173–80. Available from: https://onlinelibrary.wiley.com/doi/full/10.1002/ange.202000841

32. Schieweck BG, Jürling-Will P, Klankermayer J. Structurally Versatile Ligand System for the Ruthenium Catalyzed One-Pot Hydrogenation of CO2 to Methanol. ACS Catal [Internet]. 2020 Mar 20 [cited 2024 Apr 22];10(6):3890–4. Available from: https://pubs.acs.org/doi/full/10.1021/acscatal.9b04977

33. Roiaz M, Falivene L, Rameshan C, Cavallo L, Kozlov SM, Rupprechter G. Roughening of Copper (100) at Elevated CO Pressure: Cu Adatom and Cluster Formation Enable CO Dissociation. J Phys Chem C. 2019;123(13):8112–21.

34. Eren B, Zherebetskyy D, Patera LL, Wu CH, Bluhm H, Africh C, et al. Activation of Cu(111) surface by decomposition into nanoclusters driven by CO adsorption. Science (80- ) [Internet]. 2016 Jan 29 [cited 2024 May 12];351(6272):475–8. Available from: https://www.science.org/doi/10.1126/science.aad8868

35. Amann P, Klötzer B, Degerman D, Köpfle N, Götsch T, Lömker P, et al. The state of zinc in methanol synthesis over a Zn/ZnO/Cu(211) model catalyst. Science (80- ) [Internet]. 2022 May 6 [cited 2024 Apr 23];376(6593):603–8. Available from: https://www.science.org/doi/10.1126/science.abj7747

36. Schott V, Oberhofer H, Birkner A, Xu M, Wang Y, Muhler M, et al. Chemical Activity of Thin Oxide Layers: Strong Interactions with the Support Yield a New Thin-Film Phase of ZnO. Angew Chemie Int Ed [Internet]. 2013 Nov 4 [cited 2024 Jun 28];52(45):11925–9. Available from: https://onlinelibrary.wiley.com/doi/full/10.1002/anie.201302315

37. Liao F, Wu XP, Zheng J, Li MMJ, Kroner A, Zeng Z, et al. A promising low pressure methanol synthesis route from CO₂ hydrogenation over Pd@Zn core–shell catalysts. Green Chem. 2017;19(1):270–80.

38. Liu X, Wang H, Lu J. Recent progress in understanding the nature of active sites for methanol synthesis over Cu/ZnO catalysts. J Catal. 2024 Aug 1;436:115561.

39. Li Y, Wang Y, Zhang X, Mi Z. Thermodynamic analysis of autothermal steam and CO2 reforming of methane. Int J Hydrogen Energy. 2008;33(10):2507–14.

40. Anic K, Wolfbeisser A, Li H, Rameshan C, Fo K. Surface Spectroscopy on UHV-Grown and Technological Ni – ZrO 2 Reforming Catalysts : From UHV to Operando Conditions. 2016;1614–27.

41. Beck A, Newton MA, van de Water LGA, van Bokhoven JA. The Enigma of Methanol Synthesis by Cu/ZnO/Al2O3-Based Catalysts. Chem Rev [Internet]. 2024 Apr 24;124(8):4543–678. Available from: https://doi.org/10.1021/acs.chemrev.3c00148

42. Zhao YF, Yang Y, Mims C, Peden CHF, Li J, Mei D. Insight into methanol synthesis from CO2hydrogenation on Cu(1 1 1): Complex reaction network and the effects of H2O. J Catal. 2011;281(2):199–211.

43. Nie X, Jiang X, Wang H, Luo W, Janik MJ, Chen Y, et al.

Mechanistic Understanding of Alloy Effect and Water Promotion for Pd-Cu Bimetallic Catalysts in CO2Hydrogenation to Methanol. ACS Catal. 2018;8(6):4873–92.

44. Liu Z, Rittermeier A, Becker M, Kähler K, Löffler E, Muhler M. High-pressure CO adsorption on Cu-based catalysts: Zn-induced formation of strongly bound CO monitored by ATR-IR spectroscopy. Langmuir. 2011;27(8):4728–33.

45. Biegger P, Felder AH, Lehner M. Methanisierung von CO2 als chemischer Energiespeicher. Proc 10th Minisymp Verfahrenstechnik. 2014;

46. Bahruji H, Bowker M, Hutchings G, Dimitratos N, Wells P, Gibson E, et al. Pd / ZnO catalysts for direct CO 2 hydrogenation to methanol. J Catal. 2016;343:133–46.

47. Zhang Z, Cheng S, Liu W, Chen B, Gao X, Wang P, et al. Unraveling the regulation of Mn in Cu-ZnOx formation during methanol synthesis from syngas over Cu/ZnO/Al2O3-Mn catalysts. Appl Catal B Environ. 2023 Dec 5;338:122985.

48. Zou T, Araújo TP, Krumeich F, Mondelli C, Pérez-Ramírez J. ZnO-Promoted Inverse ZrO2-Cu Catalysts for CO2-Based Methanol Synthesis under Mild Conditions. ACS Sustain Chem Eng [Internet]. 2022 Jan 10 [cited 2024 Apr 22];10(1):81–90. Available from: https://pubs.acs.org/doi/full/10.1021/acssuschemeng.1c04751

49. Wang C, Fang Y, Liang G, Lv X, Duan H, Li Y, et al. Mechanistic study of Cu-Ni bimetallic catalysts supported by graphene derivatives for hydrogenation of CO2 to methanol. J CO2 Util. 2021 Jul 1;49:101542.

50. Yu J, Yang M, Zhang J, Ge Q, Zimina A, Pruessmann T, et al. Stabilizing Cu+ in Cu/SiO2 catalysts with a shattuckite-like structure boosts CO2 hydrogenation into methanol. ACS Catal [Internet]. 2020 Dec 18 [cited 2024 Apr 22];10(24):14694–706. Available from: https://pubs.acs.org/doi/full/10.1021/acscatal.0c04371

51. Dong X, Zhang H Bin, Lin GD, Yuan YZ, Tsai KR. Highly active CNT-promoted Cu-ZnO-Al2O3 catalyst for methanol synthesis from H2/CO/CO2. Catal Letters [Internet]. 2003 Feb [cited 2024 Apr 22];85(3–4):237–46. Available from: https://link.springer.com/article/10.1023/A:1022158116871

52. Pandit L, Boubnov A, Behrendt G, Mockenhaupt B, Chowdhury C, Jelic J, et al. Unravelling the Zn-Cu Interaction during Activation of a Zn-promoted Cu/MgO Model Methanol Catalyst. ChemCatChem [Internet]. 2021 Oct 7 [cited 2024 Apr 23];13(19):4120–32. Available from: https://onlinelibrary.wiley.com/doi/full/10.1002/cctc.202100692

53. Murthy PS, Liang W, Jiang Y, Huang J. Cu-Based Nanocatalysts for CO2Hydrogenation to Methanol. Energy and Fuels [Internet]. 2021 May 20 [cited 2024 Apr 22];35(10):8558–84. Available from: https://pubs.acs.org/doi/full/10.1021/acs.energyfuels.1c00625

54. Bahruji H, Bowker M, Hutchings G, Dimitratos N, Wells P, Gibson E, et al. Pd/ZnO catalysts for direct CO2 hydrogenation to methanol. J Catal. 2016 Nov 1;343:133–

46.

55. Zabilskiy M, Sushkevich VL, Newton MA, Krumeich F, Nachtegaal M, Bokhoven JA van. Mechanistic Study of Carbon Dioxide Hydrogenation over Pd/ZnO-Based Catalysts: The Role of Palladium–Zinc Alloy in Selective Methanol Synthesis. Angew Chemie [Internet]. 2021 Jul 26 [cited 2024 Apr 22];133(31):17190–6. Available from: https://onlinelibrary.wiley.com/doi/full/10.1002/ange.202 103087

56. Siriworarat K, Deerattrakul V, Dittanet P, Kongkachuichay P. Production of methanol from carbon dioxide using palladium-copper-zinc loaded on MCM-41: Comparison of catalysts synthesized from flame spray pyrolysis and sol-gel method using silica source from rice husk ash. J Clean Prod. 2017 Jan 20;142:1234–43.

57. Díez-Ramírez J, Díaz JA, Sánchez P, Dorado F. Optimization of the Pd/Cu ratio in Pd-Cu-Zn/SiC catalysts for the CO2 hydrogenation to methanol at atmospheric pressure. J CO2 Util. 2017 Dec 1;22:71–80.

58. Barrabes N, Cornado D, Foettinger K, Dafinov A, Llorca J, Medina F, et al. Hydrodechlorination of trichloroethylene on noble metal promoted Cu-hydrotalcite-derived catalysts. J Catal. 2009;263(2):239–46.

59. Meshesha BT, BARRABÉS N, MEDINA F, SUEIRAS JE. Polyol mediated synthesis & characterization of Cu nanoparticles: Effect of 1-hexadecylamine as stabilizing agent. In: 1st WSEAS International Conference on NANOTECHNOLOGY. 2009. p. 87–91.

60. Meshesha BT, Barrabés N, Llorca J, Dafinov A, Medina F, Föttinger K. PdCu alloy nanoparticles on alumina as selective catalysts for trichloroethylene hydrodechlorination to ethylene. Appl Catal A Gen. 2013;453:130–41.

61. Li JL, Inui T. Characterization of precursors of methanol synthesis catalysts, copper/zinc/aluminum oxides, precipitated at different pHs and temperatures. Appl Catal A Gen. 1996 Mar 28;137(1):105–17.

62. Eren B, Liu Z, Stacchiola D, Somorjai GA, Salmeron M. Structural Changes of Cu(110) and Cu(110)-(2 × 1)-O Surfaces under Carbon Monoxide in the Torr Pressure Range Studied with Scanning Tunneling Microscopy and Infrared Reflection Absorption Spectroscopy. J Phys Chem C [Internet]. 2016 May 5 [cited 2024 Jun 10];120(15):8227–31. Available from: https://pubs.acs.org/doi/abs/10.1021/acs.jpcc.6b02143

63. Qiu T, Yang JG, Bai XJ, Wang YL. The preparation of synthetic graphite materials with hierarchical pores from lignite by one-step impregnation and their characterization as dye absorbents. RSC Adv [Internet]. 2019 Apr 25 [cited 2024 May 12];9(22):12737–46. Available from: https://pubs.rsc.org/en/content/articlehtml/2019/ra/c9ra 00343f

64. Mauro M, Cipolletti V, Galimberti M, Longo P, Guerra G. Chemically reduced graphite oxide with improved shape anisotropy. J Phys Chem C [Internet]. 2012 Nov 26 [cited 2024 May 12];116(46):24809–13. Available from: https://pubs.acs.org/doi/abs/10.1021/jp307112k

65. Rameshan C, Stadlmayr W, Weilach C, Penner S, Lorenz H, Hävecker M, et al. Subsurface-Controlled CO2 Selectivity of PdZn Near-Surface Alloys in H2 Generation by Methanol Steam Reforming. Angew Chemie Int Ed [Internet]. 2010 Apr 19 [cited 2024 Jun 6];49(18):3224–7. Available from: https://onlinelibrary.wiley.com/doi/full/10.1002/anie.2009 05815

66. Weilach C, Kozlov SM, Holzapfel HH, Föttinger K, Neyman KM, Rupprechter G. Geometric arrangement of components in bimetallic PdZn/Pd(111) surfaces modified by CO adsorption: A combined study by density functional calculations, polarization-modulated infrared reflection absorption spectroscopy, and temperature-programmed desorption. J Phys Chem C [Internet]. 2012 Sep 6 [cited 2024 Jun 6];116(35):18768–78. Available from: https://pubs.acs.org/doi/abs/10.1021/jp304556s

67. Holzapfel HH, Wolfbeisser A, Rameshan C, Weilach C, Rupprechter G. PdZn surface alloys as models of methanol steam reforming catalysts: Molecular studies by LEED, XPS, TPD and PM-IRAS. Top Catal [Internet]. 2014 Sep 1 [cited 2024 Jun 10];57(14):1218–28. Available from: https://link.springer.com/article/10.1007/s11244-014-0295-3

68. Sandoval VH, Gigola CE. Characterization of Pd and Pd-Pb/α-Al2O3 catalysts. A TPR-TPD study. Appl Catal A Gen. 1996;148(1):81–96.

69. Redhead PA. Thermal desorption of gases. Vacuum. 1962;12(4):203–11.

70. Chen H, Cui H, Lv Y, Liu P, Hao F, Xiong W, et al. CO2 hydrogenation to methanol over Cu/ZnO/ZrO2 catalysts: Effects of ZnO morphology and oxygen vacancy. Fuel. 2022 Apr 15;314:123035.

71. Thang HV, Pacchioni G. Oxygen Vacancy in Wurtzite ZnO and Metal-Supported ZnO/M(111) Bilayer Films (M = Cu, Ag and Au). J Phys Chem C [Internet]. 2018 Sep 13 [cited 2024 May 7];122(36):20880–7. Available from: https://pubs.acs.org/doi/full/10.1021/acs.jpcc.8b06474

72. Fehr SM, Nguyen K, Krossing I. Realistic Operando-DRIFTS Studies on Cu/ZnO Catalysts for CO2 Hydrogenation to Methanol – Direct Observation of Mono-ionized Defect Sites and Implications for Reaction Intermediates. ChemCatChem [Internet]. 2022 Feb 8 [cited 2024 May 7];14(3):e202101500. Available from: https://onlinelibrary.wiley.com/doi/full/10.1002/cctc.2021 01500

73. Johansen KM, Tuomisto F, Makkonen I, Vines L. Formation of Zn- and O- vacancy clusters in ZnO through deuterium annealing. Mater Sci Semicond Process. 2017;69:23–7.

74. Wei X, Su W, Shi Y, Wang J, Lv P, Song X, et al. Cu0 at the Cu/ZnO interface efficiently accelerate CO2 hydrogenation to methanol over Cu/ZnO/C–P catalysts. Int J Hydrogen Energy. 2024 Mar 8;58:128–36.

75. Zhao L, Zhang L, Wu Z, Huang C, Chen K, Wang H, et al. Size Effect of Cu Particles on Interface Formation in Cu/ZnO Catalysts for Methanol Synthesis. Catalysts [Internet]. 2023 Aug 1 [cited 2024 May 7];13(8):1190. Available from: https://www.mdpi.com/2073-4344/13/8/1190/htm

76. Rahmatmand B, Rahimpour MR, Keshavarz P. Introducing a novel process to enhance the syngas conversion to

ARTICLE                                                                                           Journal Name

methanol over Cu/ZnO/Al2O3 catalyst. Fuel Process Technol. 2019 Oct 1;193:159–79.

77.  Lei H, Nie R, Wu G, Hou Z. Hydrogenation of CO2 to CH3OH over Cu/ZnO catalysts with different ZnO morphology. Fuel. 2015 Aug 15;154:161–6.

78.  Han C, Gao Y, Qin L, Cao Y, Wang S, Li J. Modulating electronic structure and exposed surface area of Cu-based catalysts by Pd doping for enhanced CO2 hydrogenation to methanol. Sep Purif Technol. 2025 Feb 19;354:128852.

79.  Reddy KP, Kim D, Hong S, Kim KJ, Ryoo R, Park JY. Tuning CO2Hydrogenation Selectivity through Reaction-Driven Restructuring on Cu-Ni Bimetal Catalysts. ACS Appl Mater Interfaces [Internet]. 2022 [cited 2024 Jul 28]; Available from: https://pubs.acs.org/doi/abs/10.1021/acsami.2c20832

80.  Föttinger K, Schlögl R, Rupprechter G. The mechanism of carbonate formation on Pd–Al $_2$ O $_3$ catalysts. Chem Commun. 2008;3(3):320–2.

81.  Wu XK, Xia GJ, Huang Z, Rai DK, Zhao H, Zhang J, et al. Mechanistic insight into the catalytically active phase of CO2 hydrogenation on Cu/ZnO catalyst. Appl Surf Sci. 2020 Sep 30;525:146481.

82.  Xu J, Su X, Liu X, Pan X, Pei G, Huang Y, et al. Methanol synthesis from CO2 and H2 over Pd/ZnO/Al2O3: Catalyst structure dependence of methanol selectivity. Appl Catal A Gen. 2016 Mar 25;514:51–9.

83.  Zabilskiy M, Sushkevich VL, Palagin D, Newton MA, Krumeich F, van Bokhoven JA. The unique interplay between copper and zinc during catalytic carbon dioxide hydrogenation to methanol. Nat Commun 2020 111 [Internet]. 2020 May 15 [cited 2024 Mar 4];11(1):1–8. Available from: https://www.nature.com/articles/s41467-020-16342-1

84.  Ojelade OA, Zaman SF, Daous MA, Al-Zahrani AA, Malik AS, Driss H, et al. Optimizing Pd:Zn molar ratio in PdZn/CeO2 for CO2 hydrogenation to methanol. Appl Catal A Gen. 2019 Aug 25;584:117185.

85.  Azhari NJ, Erika D, Mardiana S, Ilmi T, Gunawan ML, Makertihartha IGBN, et al. Methanol synthesis from CO2: A mechanistic overview. Results Eng. 2022 Dec 1;16:100711.

86.  Grabow LC, Mavrikakis M. Mechanism of methanol synthesis on cu through CO2 and CO hydrogenation. ACS Catal [Internet]. 2011 Apr 1 [cited 2024 Jul 21];1(4):365–84. Available from: https://pubs.acs.org/doi/abs/10.1021/cs200055d

87.  Mravak A, Vajda S, Bonačić-Koutecký V. Mechanism of Catalytic CO2Hydrogenation to Methane and Methanol Using a Bimetallic Cu3Pd Cluster at a Zirconia Support. J Phys Chem C [Internet]. 2022 Nov 3 [cited 2024 Jul 21];126(43):18306–12. Available from: https://pubs.acs.org/doi/full/10.1021/acs.jpcc.2c04921

88.  Lopes Martins JB, Longo E, Rodríguez Salmon OD, Espinoza VAA, Taft CA. The interaction of H2, CO, CO2, H2O and NH3on ZnO surfaces: An Oniom Study. Chem Phys Lett. 2004;400(4–6):481–6.

## Data availability statement

The data supporting this article have been included as part of the Supplementary Information.

**RSC Sustainability Accepted Manuscript**